Molecular Weight Dependent Structure and Charge Transport in MAPLE-deposited Poly(3-hexylthiophene) Thin Films

Ban Xuan Dong,[1,┼,] * Mitchell Smith,[2] Joseph Strzalka,[3] Huanghe Li,[4] Anne McNeil,[2,4] Gila E. Stein[5] and Peter F. Green[1,4,⊥,*]

[1]Department of Materials Science and Engineering, Biointerfaces Institute, [2]Department of Chemistry, [4]Macromolecular Science and Engineering, University of Michigan, Ann Arbor, MI 48109, USA

[3]X-Ray Science Division, Argonne National Laboratory, Argonne, Illinois, 60439, USA

[5]Department of Chemical and Biomolecular Engineering, University of Tennessee, Knoxville, TN 37996, USA

[⊥]National Renewable Energy Laboratory, 15013 Denver W Pkwy, Golden, CO 80401, USA.

[┼]Current Address: Institute for Molecular Engineering, The University of Chicago, Chicago, IL, 60637, USA

Correspondence to: Ban Xuan Dong (Email: banxdong@umich.edu) and Peter F. Green (Email: pfgreen@umich.edu).

((Additional Supporting Information may be found in the online version of this article.))

ABSTRACT

In this work, poly(3-hexylthiophene) (P3HT) films prepared using the matrix-assisted pulsed laser evaporation (MAPLE) technique are shown to possess morphological structures that are dependent on molecular weight (MW). Specifically, the structures of low MW samples of MAPLE-deposited film are composed of crystallites/aggregates embedded within highly disordered environments, whereas those of high MW samples are composed of aggregated domains connected by long polymer chains. Additionally, the crystallite size along the side-chain (100) direction decreases, whereas the conjugation length increases with increasing molecular weight. This is qualitatively similar to the structure of spin-cast films, though the MAPLE-deposited films are more disordered. In-plane carrier mobilities in the MAPLE-deposited samples increase with MW, consistent with the notion that longer chains bridge adjacent aggregated domains thereby facilitating more effective charge transport. The carrier mobilities in the MAPLE-deposited simples are consistently lower than those in the solvent-cast samples for all molecular weights, consistent with the shorter conjugation length in samples prepared by this deposition technique.

KEYWORDS: MAPLE, conjugated polymers, molecular weight dependence, GIWAXS, UV-vis absorption.

INTRODUCTION

Guided by molecular design principles, conjugated polymers may be synthesized to possess a diverse range of physical properties, rendering them useful for commercially diverse applications, including xerography,[1] organic light-emitting diodes (OLEDs),[2,3] organic thin-film transistors (TFTs)[4] and organic photovoltaics (OPVs).[5,6] Unlike their inorganic semiconductor counterparts, conjugated polymers offer advantages of solution processability and mechanical flexibility. Moreover, they have the added advantage that through exploiting molecular design principles, conjugated polymers may be synthesized to possess a diverse range of physical properties.

The physical properties and performance of conjugated polymer-based devices greatly depends on morphology -charge carrier mobilities depend on details of the morphological structure. The morphology is determined by factors that include the chemical structure of the polymers, the preparation methods, pretreatment and wettability of the substrates, the solvent used for film deposition and the post-annealing – solvent vapor and temperature processes.[7–12] With regard to methods of preparation, thin films of conjugated polymers are typically deposited using solution-based methods, which offer the advantages of simplicity, low-cost and potential scale-up. Nevertheless, solution-based direct fabrication methods have inherent challenges; it is difficult to fabricate layered nanostructures, and preparing films on substrates with poor wettabilities. A novel vacuum-assisted fabrication technique called matrix-assisted pulsed laser evaporation (MAPLE) has been used to fabricate films of polymers, proteins, small molecules and nanoparticles[13–17] without the aforementioned limitations of solution-deposition, and with added advantages such as fabricating ultrastable polymer glasses or growing polymer crystallites with an extremely slow and controllable rate.[18,19] Unlike other vacuum deposition techniques of polymers, the film deposition process in MAPLE involves the absorption of light with a specific wavelength from a laser by a frozen dilute polymer/solvent mixture. Specifically, the sacrificial host solvent is chosen such that it absorbs the majority of the laser energy, thereby altogether avoiding the photochemical degradation of the guest polymer. Prior studies have demonstrated that the chemical structure, molecular weight and molecular weight distribution are maintained through judicious choice of the MAPLE deposition parameters.[20–22]

MAPLE has successfully been used to grow thin conjugated polymer films for various organic electronic applications.[20–30] Our prior research has begun to elucidate fundamental connections between crystallization, morphology, electronic structure and carrier transport in MAPLE-deposited conjugated polymer films.[23,29,31,32] An important, yet poorly understood problem is understanding the role of molecular weight on the structure and physical properties of conjugated polymers deposited by the MAPLE technique. To this end, we report a study of the connection between the structure and in-plane charge transport properties of poly(3-hexylthiophene) (P3HT) films of varying molecular weights (M_n: 2.8 kDa, 4.7 kDa, 10.8 kDa and 21.5 kDa) deposited by both MAPLE and conventional spin-casting techniques. Using grazing-incidence wide angle X-ray scattering (GIWAXS) and UV-vis absorption spectroscopy, we show that for the same molecular weight, MAPLE-deposited samples were more disordered, with smaller crystallite/aggregate sizes in comparison to spin-cast films. The effects of MW on crystallite sizes, disorder parameters, and conjugation lengths of MAPLE-deposited films are very similar to those of spin-cast films. However, the effects of MW on surface topographies are very different for the two processes. A comprehensive UV-vis absorption study supports the notion that similar to spin-cast samples, the low MW samples of MAPLE-deposited films are composed of crystallites/aggregates embedded within a

highly disordered (amorphous) environment, whereas the high MW samples comprise long polymer chains that bridge multiple aggregated regions. This bridging that occurs within the high MW samples facilitates easier movement of charges throughout the films via various percolation pathways, thereby increasing carrier mobilities as revealed by the complementary in-plane carrier mobility measurements.

EXPERIMENTAL

Polymer synthesis

P3HT with different molecular weights were synthesized using catalyst transfer polycondensation (CTP) methods following the previously reported procedure.[33–36] More details of the synthesis method and GPC traces are listed in the Supporting Information. M_w, M_n and the polydispersity index $Đ$ of the four polymer batches synthesized in this work is summarized in Table 1.

Table 1: M_n, M_w and polydispersity index $Đ$ of the polymer batches synthesized in this work

M_n (kDa)	M_W (kDa)	$Đ$
2.8	3.6	1.3
4.7	6.0	1.3
10.8	15.1	1.4
21.5	28.0	1.3

Samples preparation

All substrates were unltrasonicated in an Alconox® detergent solution, DI water, acetone, boiling Hellmanex® solution and 2-propanol for 5 min each, followed by UV-ozone cleaning for 20 min. UV-vis absorption measurement were performed on polymer films supported by glass substrate. Thin film transistor (TFT), grazing incidence wide angle X-ray scattering (GIWAXS) and atomic force microscopy measurements were performed on polymer films deposited on highly doped Si with 300 nm of thermally-grown SiO_2 (SiO_2/Si) substrates. Prior to polymer deposition, a self-assembled monolayer of octadecyltrichlorosilane (OTS) (Sigma-Aldrich) was grown on all substrates by immersing the bare substrate in a mixture of OTS and hexadecane (1:250 by volume) for 14 hours while stirring.

Solutions of P3HT at different molecular weights were prepared by dissolving the polymers in *o*-dichlorobenzene and shaken overnight before filtering with a 0.45 µm filter. The filtered solutions were then spun onto the prepared substrates at 600 rpm for 3 min to make spin-cast films. For each molecular weight, the P3HT concentrations were fine-tuned to get the final film thickness of approximately 100 nm.

Our MAPLE deposition system built by PVD Products is equipped with an Er:YAG laser (Quantel) that produces a peak wavelength of 2.94 µm. In order to deposit thin conjugated polymer films, we utilized the emulsion-based MAPLE method. In this approach, a 5 mg/ml of solution of P3HT and a good organic solvent *o*-dichlorobenzene was mixed with benzyl alcohol and deionized (DI) water (containing 0.005 wt.% sodium dodecyl sulfate surfactant) at the 1:0.3:3 ratio. The mixture was then shaken and ultrasonicated to generate a homogeneous emulsion. The emulsion was injected into a pre-cooled target cup (ca.−150 °C) inside the deposition target chamber and "flash-frozen." The chamber was then pumped down to a pressure below 2×10^{-5} Torr prior to deposition. To maintain uniform ablation, the target cup and the substrate holder were rotated at a constant angular velocity, while the laser

(fluence ~1.3 J/cm^2 at a repetition rate of 5 Hz)

was rastered across the surface of the target material. Each substrate was suspended face-down at a height of 5.5 cm above the target.

The deposition time was 5 hours. The thickness of each MAPLE-deposited film was 100 nm, the same thickness as the spin-cast films, as confirmed using AFM and spectroscopic ellipsometry.

Grazing incidence wide angle X-ray scattering (GIWAXS)

GIWAXS measurements were performed at beamline 8-ID-E of the Advanced Photon Source (Argonne National Laboratory) with 10.86 keV (λ = 0.11416 nm) synchrotron radiation.[31,37] The measurement time was 4 sec per frame and samples were enclosed and measured inside a low vacuum chamber (10^{-3} mbar) to minimize concerns about radiation damage as well as to prevent extraneous scattering from ambient air. During GIWAXS measurements, the samples were tilted at an angle of incidence of 0.14° with respect to the beam. This angle was chosen to be above the critical angle of the polymer films (0.129°) yet below the critical angle of the Si substrates (0.166°) in order to probe the entire thickness of the polymer films. Four data sets were taken from 4 different spots on each sample; the data sets were averaged to further enhance the signal-to-noise ratio. All scattering was recorded using a Pilatus 1MF pixel array detector (pixel size = 172 μm) positioned 228 mm from the sample. Each data set was stored as a 981x1043 32-bit tiff image with 20-bit dynamic range. The Pilatus detector has rows of inactive pixels at the border between detector modules. To fill these gaps, after each measurement the detector was moved to a new vertical direction and the measurement on each spot was repeated. The gaps were filled by combining the data from two detector positions. This procedure was implemented using the GIXSGUI package for MATLAB.[38] The signals were output as intensity maps in (q_y, q_z)-space also by using the GIXSGUI package. The GIXSGUI package was used to correct the images for detector nonuniformity, detection efficiency, the polarization effect and solid-angle variation.

To construct the partial pole figure of each sample, wedge cuts with an angular breadth of 1° were extracted from the GIWAXS 2D diffraction pattern using GIXSGUI. Each wedge cut was first fit to an empirical baseline function to subtract the background intensity and amorphous scattering. The background-subtracted wedge cut was then fit to a Voigt function to extract the integrated intensity as well as the full width at half maximum (FWHM) of the reflection of interest (100). The integrated intensity of each peak was reported as a function of the polar angle χ between the scattering vector and pole vector.

Ultraviolet-visible (UV-vis) absorption spectroscopy

The ultraviolet–visible (UV–vis) absorption spectroscopy measurements were performed using a Lambda 750 UV/vis/ NIR Spectrophotometer (PerkinElmer Inc.) and analyzed with the Spano model. Additional information is included in the Supporting Information.

In-plane mobility measurements

Top-contact, bottom-gate transistor configurations were used to fabricate transistors on which in-plane mobility measurements were performed. The size of the device used in our work was ca. 0.5 x 0.5 inch. Each thin film transistor was prepared using OTS-treated substrate. After deposition of polymer films, source and drain silver electrodes (Kurt J. Lesker) were vacuum-deposited on top of the polymer film at a rate of 0.5 A/s; each transistor had a channel length and width of 50 μm and 500 μm, respectively. In-plane hole mobilities (μ) were measured using the Agilent 4156C Parameter Analyzer. The hole mobility was extracted from the drain current I_{DS} by fitting the transfer curve in the saturation regime (V_D = -80 V) using the following equation:

$$I_{DS} = \frac{WC_i}{2L}\mu(V_g - V_t)^2 \quad (1)$$

In this equation, W and L are the channel width and length, C_i = 10 nF/cm^2 is the capacitance per unit area of the insulating SiO_2 layer, V_g and V_t are the gate and threshold voltage, respectively. The mobility experiments were conducted in a nitrogen-filled glovebox at room temperature.

Atomic Force Microscopy (AFM)

Topographical images of the top and buried interfaces of P3HT films were probed using an Asylum Research MFP-3D stand-alone AFM in tapping mode with a CT300-25 Aspire probe (spring constant 40 N/m and radius of curvature of 8 nm).

RESULTS AND DISCUSSIONS

GIWAXS Patterns

Shown in Figure 1 are GIWAXS patterns of spin-cast and MAPLE-deposited films for different P3HT MWs on OTS substrates. For all samples, we observe the (100) side-chain diffraction peak predominantly in the out-of-plane direction and the (020) π-stacking diffraction peak predominantly in the in-plane direction, suggesting bias towards the edge-on orientation of polymer crystallites. In the diffraction pattern of the spin-cast sample at M_n = 2.8 kDa, besides the commonly observed (*h*00) and (0*k*0) diffraction peaks, we also detect two other series of diffraction peaks at q_y~1.1 Å^{-1} and ~1.6 Å^{-1} as indicated in Figure 1a. The appearance of extra diffraction peaks has been widely observed in low MW spin-cast P3HT samples before, which originates from the more ordered structure of low MW samples.[8,39–41] The GIWAXS pattern of this sample is in fact very similar to the one reported by Himmelberger et al. for films of P3HT with MW ~ 1.8 kDa.[41]

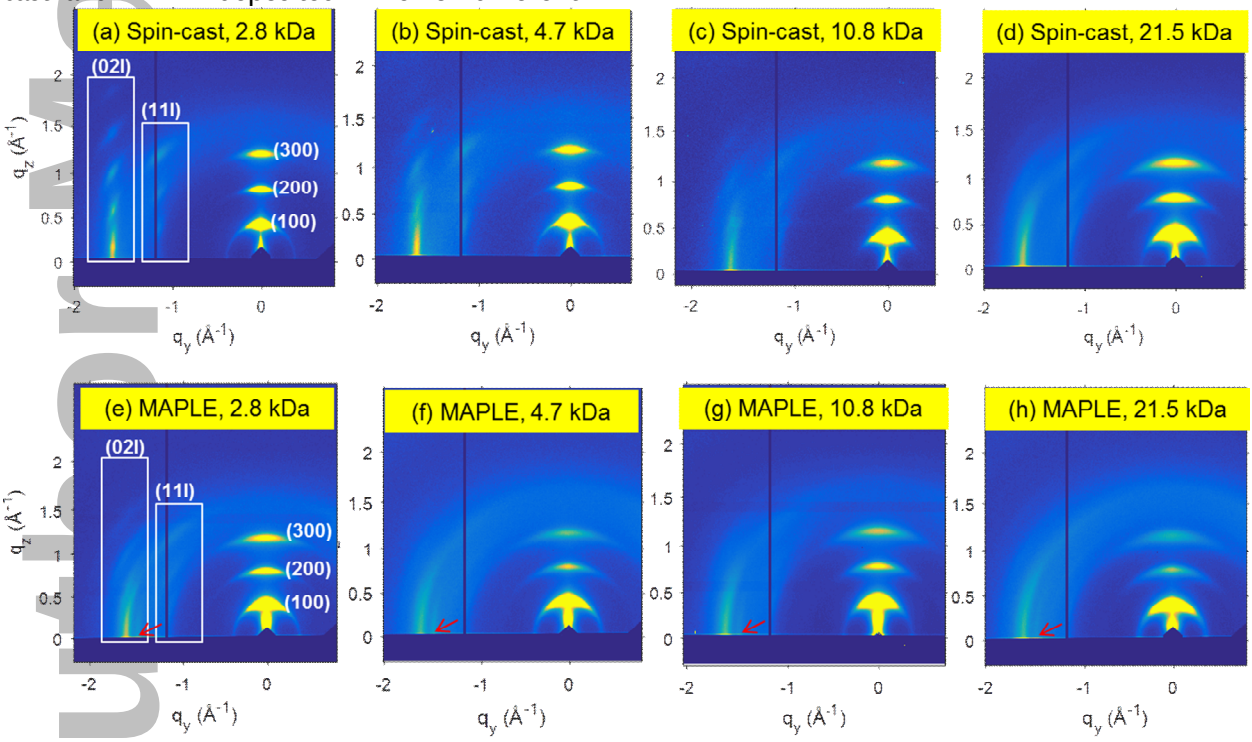

Figure 1: GIWAXS patterns of (a)-(d) spin-cast and (e)-(f) MAPLE-deposited samples at different MWs. Peak indexing shown in the GIWAXS patterns of the lowest MW for both MAPLE and spin-cast samples was performed following previous work of Himmelberger et al.[41] The red arrows in figure (e)-(h) indicate the mixed-index peaks observed in MAPLE-deposited samples but not in spin-cast samples.

Based on their analysis, we assign the peaks at q_y~1.1 Å^{-1} and ~1.6 Å^{-1} as (11*l*) and (02*l*) peaks, respectively, where *l* = 0, 1, 2, 3…The diffraction patterns of spin-cast samples at other MWs appear qualitatively similar but the peaks become broader along both q and χ (polar angle) with increasing MW. This peak broadening indicates that as the MW increases, the film structure becomes more disordered and the polymer crystallite orientation becomes more random. Nevertheless, the similarity of the diffraction patterns for all MWs of spin-cast samples suggests that the unit cell of the low and high MW samples are likely comparable, so the information retrieved from low MW could be applicable to higher MW materials.[41]

For the same molecular weight, the diffraction patterns determined from spin-cast films are similar as those of MAPLE-deposited films; the peak shapes are however more diffuse. This suggests that MAPLE-samples have similar unit cell as spin-cast samples, but the structure is more disordered, which is consistent with our previous studies for a high MW commercial P3HT.[23,29] This trend can be seen clearly by comparing the low MW data in Figure 1e and 1a, where both types of films show the higher order (11*l*) and (02*l*) peaks at q_y~1.1 Å^{-1} and ~1.6 Å^{-1} ; the peaks are however much broader along the q and (angular) directions with MAPLE-deposition compared to spin-cast samples. As the MW increases, the extent of disorder increases with either deposition method, and the extent of disorder at fixed MW is consistently larger in MAPLE-deposited films compared to spin-cast analogs. Additionally, some of the (11*l*) and (02*l*) diffraction peaks appeared at M_n = 2.8 kDa are not clearly visible at higher MW samples, possibly due to the overlapping of adjacent peaks. One distinction in the GIWAXS data for between the MAPLE deposited and spin cast techniques is the appearance of an extra diffraction peak in all MAPLE-deposited samples at q~1.48 Å^{-1}; this is indicated by the red arrows in Figure 1(e)-(h). While this peak was not observed in the spin-cast samples in our study, it has been detected in spin-cast samples fabricated using chloroform,[42,43] a solvent known to produce a highly disordered morphologies due to its high volatility.[10] The appearance of this peak in MAPLE-deposited samples in this study and in our prior study[29] suggests that there is a higher degree of chain folding and twisting in P3HT films deposited using the MAPLE technique compared to the spin-cast P3HT films.

Partial Pole Figures of (100) Diffraction Peak

To quantitatively measure the distribution of polymer crystallite orientations within the samples, we constructed the partial pole figures of (100) reflection of all samples using the previously reported procedures.[29,31] Figure 2 depicts the normalized, geometrically corrected partial pole figures of (a) spin-cast and (b) MAPLE-deposited samples at different MWs. Here, χ is the polar angle between the substrate normal and the scattering vector along the side-chain direction q_{100}. We note that due to the geometry of the GIWAXS measurement, data for χ < 2° are not resolvable in our GIWAXS measurement, as indicated by the shaded areas in Figure 2.[31]

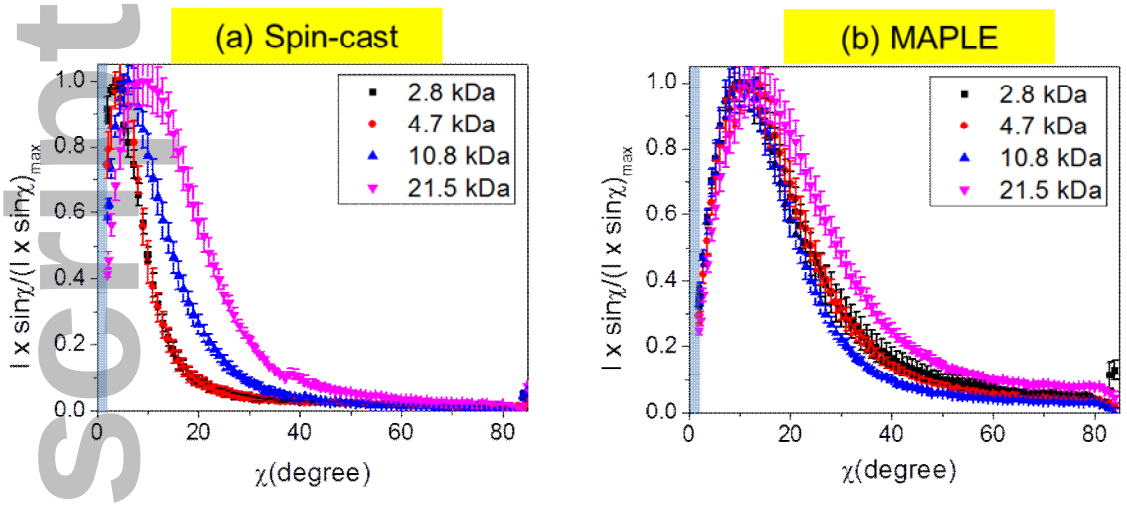

Figure 2: Normalized partial pole figures of (100) reflection in (a) spin-cast and (b) MAPLE-deposited samples at different molecular weights. The shaded areas reflect the non-measurable regimes in GIWAXS measurement. The error bar was calculated from the uncertainty of the peak fitting.

It is evident that all samples exhibit a large population of crystallites with average orientation near χ = 5°-15°, suggesting a bias towards the edge-on orientation. In spin-cast samples, the distribution along χ becomes broader with increasing MW, indicative of more random orientation of polymer crystallites. Moreover, the center of the distribution shifts to a higher value of χ, meaning that on average the side-chain within the polymer crystallites tends to orient away from the substrate normal with increasing MW. The trend in MAPLE-deposited samples is similar but not as strong as in spin-cast samples. In MAPLE-deposited samples, the pole figure distributions are almost identical within experimental error for M_n at or below 10.8 kDa but slightly broader at M_n = 21.5 kDa. These results quantify the trends evident from inspection of the raw detector images in Figure 1.

Crystallite Dimension and Disordered Parameters Measured by GIWAXS

It is well-known that the broadening (or peak breadth) of a diffraction peak in GIWAXS measurement could originate from either crystallite size or cumulative disorder, or a combination of both.[44] Therefore, in the first step we use the Williamson-Hall analysis to separate the contributions of crystallite size and disorder parameter across the side-chain stacking direction (100) of the samples. In brief, by fitting the full width at half-maximum (FWHM) of the (*h*00) reflections as a function of h^2 to a linear fit, the slope of the fit can be related to the disorder parameter while the intercept is inversely proportional to the average crystallite size.[45] Here, it is worth mentioning that there is an artificial source of peak broadening due to geometric smearing effect, as pointed out in our recent study.[31] This effect is *q*-dependent and quite substantial in GIWAXS measurement because of the large footprint of the X-Ray beam. Therefore, we perform additional geometric correction for the FWHM using previously reported calculations,[31,46] the details of which are shown in Supporting Information. Similar crystallite size/disorder analysis on the (020) π-stacking peak is unfortunately not possible due to the lack of higher order diffraction peaks of this reflection. Nevertheless, it has been shown that the broadening of the (020) peak in P3HT is mostly due to cumulative disorder.[40,47] Thus we can estimate the disorder parameter (paracrystallinity) *g* of the (020) reflection using the peak breadth Δq and peak position q_0 according to $g \approx [\Delta q / (2\pi/q_0)]^{1/2}$.[40,47] The MW evolution of crystallite dimension and disorder

parameters along (100) and (020) directions are plotted in Figure 3.

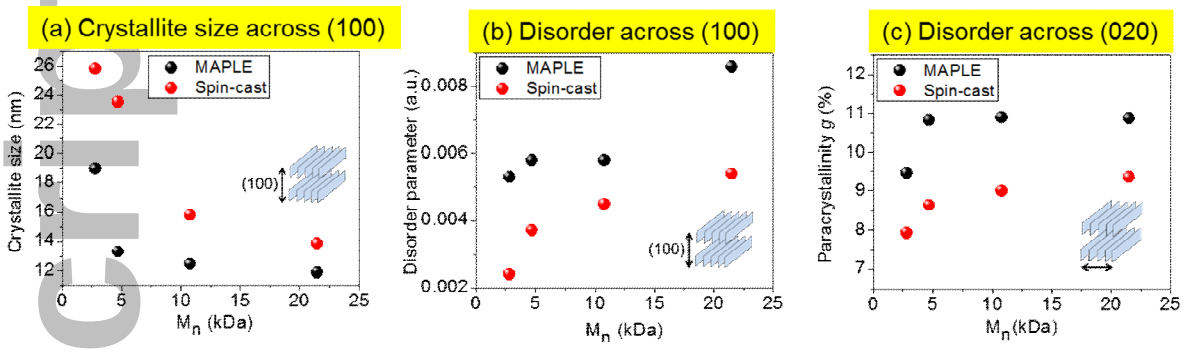

Figure 3: (a) The crystallite size across side-chain (100) direction and the disorder parameters across (b) side-chain and (c) π-stacking (020) direction. Peak shape analysis of (100) peaks was performed on data extracted from the wedge cuts taken at the detector angle ω = 0° (vertical direction), whereas analysis of (020) peaks was performed on data extracted from the wedge cuts taken at the detector angle ω = 83° (nearly horizontal direction).

As shown in Figure 3, for the same MW, the crystallite size is smaller but the extent of the disorder always larger in MAPLE-deposited samples. Along the side-chain direction (100), we observe a substantial decrease in the average crystallite size -from 26 nm to 14 nm in spin-cast samples and from 19 nm to 12 nm in MAPLE-deposited samples going from the lowest to the highest MW (Figure 3a). Together with the decrease in crystallite size along the (100) direction, we also observe the increase in disorder along (100) direction (Figure 3b) and π-stacking (020) direction (Figure 3c) for both MAPLE and spin-cast samples. That the crystallite size decreases and the degree of disorder across side-chain and π-stacking directions increases with MW is well-known for solution-processed conjugated polymer films.[8,40,47] The increasing disorder along the side-chain and π-stacking directions is believed due to the increase in degree of chain folding with increasing MW, a typical characteristic of semicrystalline polymers.[48] The higher degree in chain folding manifests a larger population of re-entrant folded chains in a crystal domain, exerting more stress on the molecular packing. This likely results in more disorder and smaller crystallite size along intermolecular packing directions (100) and (020).[49] The fact that similar behavior is observed in MAPLE-deposited films suggests that the same chain-folding phenomenon would also be responsible for their MW dependent behaviors.

UV-vis Absorption Spectra

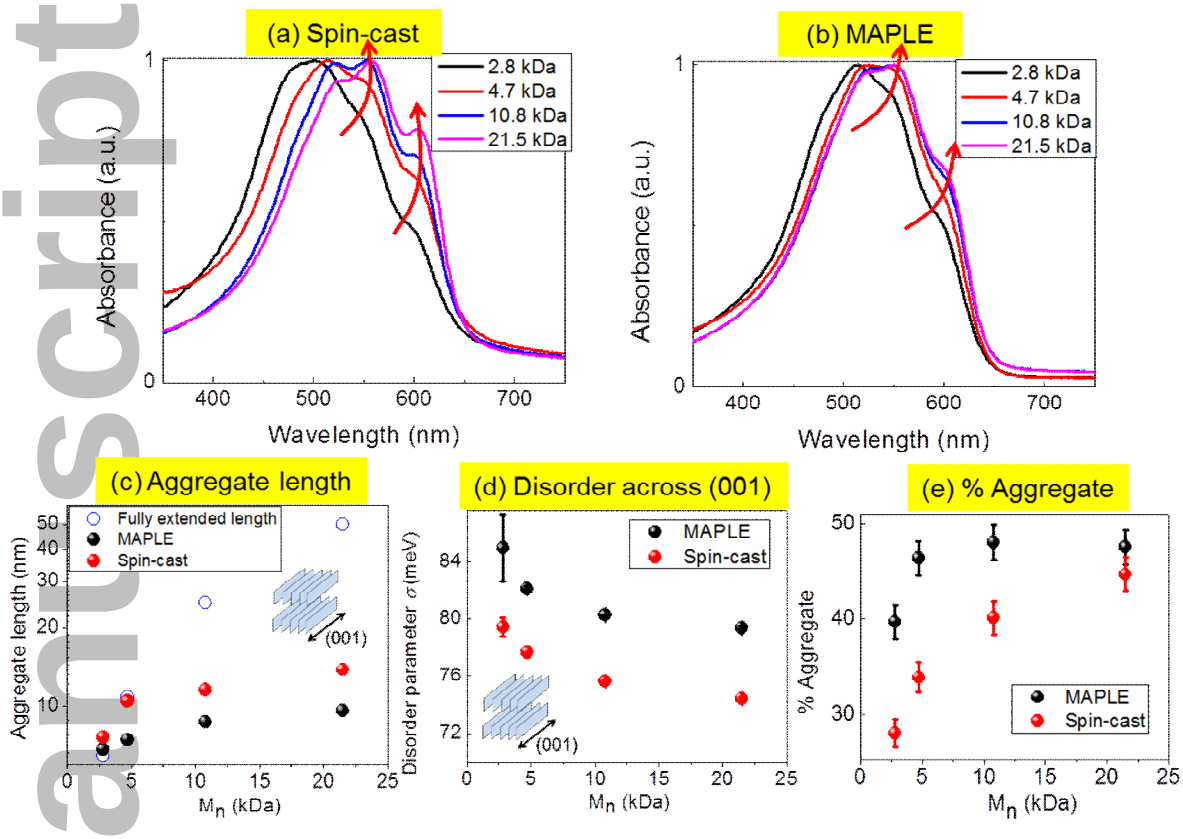

Figure 4: UV-vis absorption spectra of (a) Spin-cast and (b) MAPLE-deposited samples. (c) The aggregate length, (d) disorder parameter and (c) the aggregate fraction as a function of MW.

Information from UV-vis absorption spectra was used to calculate aggregate sizes, the fraction of aggregates as well as the disorder parameter along the backbone direction (001). It is important to note that because absorption in conjugated polymers occurs along the chain backbone, the UV-vis absorption measurement is more sensitive to polymer chains with in-plane alignments. Nevertheless, our previous investigation using spectroscopic ellipsometry suggested the polymer chains both in MAPLE and spin-cast samples exhibited tendencies toward orienting parallel to the substrate.[29] Thus we believe that the result from our UV-vis absorption measurement discussed herein reflects the absorption of the majority of the aggregates within the samples. As shown in Figure 4a and b, for both MAPLE and spin-cast samples, the intensity of the vibronic shoulders at ca. 550 nm and 600 nm, respectively, that correspond to aggregate absorption of P3HT[50] increases with increasing MW, as indicated by the red arrows. This is suggestive of the growing fraction of the aggregates within the polymer films with increasing MW. The total absorption may be further deconvoluted into individual peaks by applying the Spano model, from which the exciton bandwidth W and the disorder parameter σ can be calculated.[51,52] Then using the exciton bandwidth W we extract the aggregate length with the aid of a model developed by Gierschner et al. (see more details in Supporting Information).[53,54]

Similar to data shown in Figure 3, for the same MWs, the aggregates are always larger in spin-cast sample and the disorder parameter σ is always lower, suggesting a higher degree of disorder in MAPLE-deposited samples. Interestingly, for both MAPLE and spin-cast samples, the MW dependence of the aggregate lengths and disorder parameters along the (001) direction (Figure 4c, d) is opposite to the

dependence in the (100) and (020) directions (Figure 3) -the aggregate length increases but the disorder parameter decreases with increasing MW. This suggests that a higher degree of chain folding for longer chains induces disorder along the intermolecular packing directions; it nevertheless does not affect intramolecular disorder. For spin-cast films, the aggregate length increases from ca. 8 nm at the lowest MW to ca. 14 nm at the highest MW, whereas the aggregate length increases from ca. 7 nm to ca. 10 nm for MAPLE-deposited samples (Figure 4c). To highlight the chain conformations at different MWs, we also plot in Figure 3c the fully extended length, defined as the full length of the aggregate at each MW in the absence of distortion/defects along the polymer chain. We observe that for spin-cast samples of chains with molecular weights at or below 4.7 kDa, the aggregate length is almost the same as the fully extended length, indicating that at these MWs the polymer chains inside the aggregates are nearly planarized, consistent with minimal distortions across the polymer backbone. Similar behavior is observed for MAPLE-deposited sample at M_n = 2.8 kDa. For higher MWs, the aggregate length is significantly lower than the full extended length of the polymer chains (note the log scale of *y* axis), suggesting that a single polymer chain at high MW not only consists of planarized/aggregated segments but also coiled/amorphous segments as well. With regard to the highest M_n = 21.5 kDa, the aggregate length is only ca. 28% of the fully extended length in spin-cast sample and ca. 20% in MAPLE deposited samples.

The fraction of aggregate within the samples is calculated by comparing the absorption strength of the amorphous and aggregate portions using the approach by Clark et al,[55] the result of which is shown in Figure 4e. Interestingly, despite the highly disordered structure, the aggregate fraction in MAPLE-deposited samples is always higher than that of spin-cast films at the same MW. Notably, at M_n = 2.8 kDa the fraction of aggregate in MAPLE-deposited sample is ca. 40% compared to ca. 28% in spin-cast sample. As MW increases the aggregate fraction in both MAPLE and spin-cast samples increase accordingly and the differences between MAPLE and spin-cast samples diminish, consistent with our previous finding.[23] At M_n = 21.5 kDa the aggregate fractions in MAPLE and spin-cast samples are ca. 48% and 45%, respectively. The higher aggregate fraction in MAPLE-deposited films could be interpreted as follows. As described in the experimental section, the target emulsion is fabricated by first adding benzyl alcohol (BnOH) into the P3HT solution in dichlorobenzene, followed by adding deionized (DI) water and then shaken and ultrasonicated. Addition of BnOH is necessary to suppress the sublimation of dichlorobenzene in the vacuum chamber prior to MAPLE deposition as well as to create a homogeneous emulsion.[22] BnOH can also promote chain aggregations in P3HT solution due to the poor solubility of P3HT in it. This is apparent from the appearance of the aggregate shoulder in UV-vis absorption spectra measurement of dilute P3HT solution after adding BnOH, as shown in Supporting Information. Although we are not able to measure the absorption of the emulsion due to its opaque nature, we expect even higher aggregate contents after ultrasonicating because sonication has been known to assist self-assembly of P3HT chains in solution.[56,57] Therefore, it is likely that there exists a substantial amount of pre-formed aggregates inside the frozen target prior to film deposition. These aggregates could either be transported to the substrate intact or serve as nuclei and continue to grow during the deposition process before reaching the substrate. This results in the higher fraction of aggregates in MAPLE-deposited films compared to their spin-cast analogs.

Using the MW dependence of aggregate length and aggregate fraction, we were able to infer additional information about the morphology of the samples. As mentioned above, for both MAPLE and spin-cast samples, for low MWs we

considered the polymer chains within the aggregates to be fully extended and conjugated, yet the aggregate fraction is low. We therefore conclude that for low MWs, both MAPLE and spin-cast samples must consist of a large portion polymer chains that is completely amorphous. On the other hand, at higher MWs the aggregate length is substantial smaller than the fully extended length, but the aggregate fraction is higher compared to low MW samples. This observation implies that the polymer chains at high MW likely bridge multiple aggregates together. For example, the aggregate length of spin-cast sample at 21.5 kDa is ca. 28% of the total extended length but the total aggregate fraction is ca. 45%. Thus on average one single chain must participate in 2 aggregates at this MW to account for the differences.[54] MAPLE-deposited samples exhibit similar morphological transitions with increasing MW, but since they have shorter conjugation lengths and higher fractions of aggregates at each MW, the polymer chains in MAPLE-deposited sample should consist of more conjugated segments compared to the spin-cast analogs.

AFM measurement

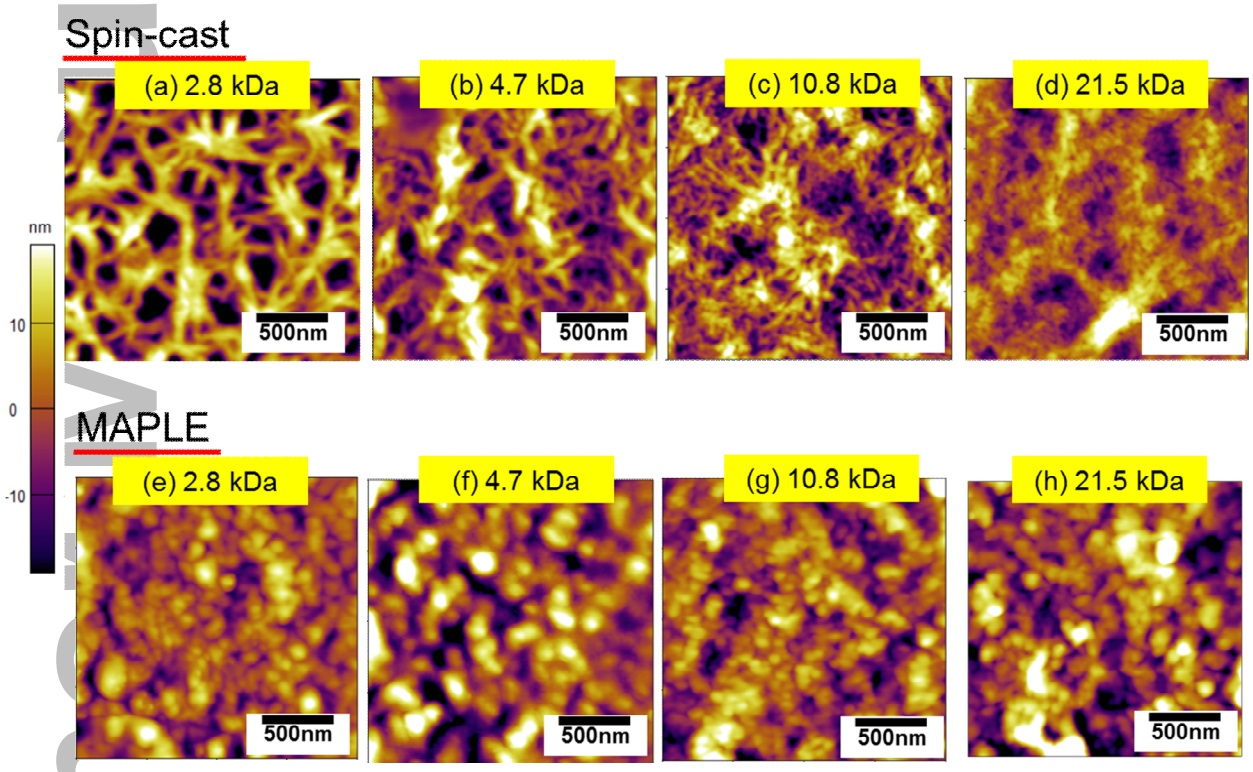

Figure 5: AFM images of (a)-(d) spin-cast samples and (e)-(f) MAPLE-deposited samples at different MWs.

The surface topographies of both MAPLE and spin-cast samples were measured using AFM. As depicted in the top row of Figure 5, the surface topographies of the spin-cast samples are strongly dependent on molecular weight. The spin-cast samples contain crystalline fibers whose widths decrease with increasing MW. The average widths of the fibers are 120 nm ± 55 nm, 85 nm ±25 nm and 70 nm ±20 nm for the 2.8 kDa sample, 4.7 kDa sample and 10.8 kDa sample, respectively. The sample of M_n = 21.5 kDa also exhibits fiber-like structure with the average fiber width of 60 nm ± 15 nm, though the structure is not as well defined as those of the lower MW samples. The trends observed in our study here are consistent with previous published reports describing spin-cast samples, where the low MW films exhibit highly

ordered fiber-like structure and the high MW films were less ordered.[8,58] In stark contrast, the topographies of the MAPLE-deposited samples exhibit no discernable MW dependent behavior. Their topographies are globular, originating from the mechanisms of target ablation -the polymer-solvent clusters are ejected toward the substrate. The average diameters of the globules in all samples are approximately 150 nm ± 50 nm, which are significantly larger than the fully extended chain length of all MWs.

The differences between the topographies of spin-cast and MAPLE-deposited samples may be understood from the following. During the spin-casting process, as the solvent evaporates and the polymer chains solidify, the first step of crystallization involves the formation/nucleation of polymer aggregates. This is then followed by the continuous development of the nucleated aggregates to form larger size aggregates and crystallites.[59,60] Due to their lower viscosity both in solution and solid states, the chains in low MW materials are more mobile compared to their high MW counterparts. In our study we fabricated spin-cast films using a high boiling point solvent (*o*-dichlorobenzene) with relatively slow spinning rate (600 rpm); hence the solvent evaporation time is sufficiently long for the development of large-sized, macroscopic-scale fiber structures in low MW samples. This leads to the strong MW dependence of surface topography in spin-cast films. Experiments and simulations demonstrate that MAPLE deposition involves the ejection of polymer-solvent clusters toward the substrate after the laser pulses superheat the frozen target beyond the ablation threshold. The majority of solvent molecules inside the polymer-solvent clusters are removed during transport from target to substrate, forming polymer globules.[61,62] While it is remains unclear whether the aggregates/crystallites form before or after reaching the substrate,[29,31] the duration of transport from target to the substrate during MAPLE deposition is notably very fast (on the order of tens of microsecond).[61] Under such condition, the solvent is rapidly removed, preventing low MW chains from forming well-defined fiber structures as observed in the case of spin-cast samples. We suspect this is the reason why the surface of MAPLE-deposited samples all exhibit typical globular morphology regardless of the MW. This hypothesis is further corroborated by the observed differences in crystallite/aggregate size (Figure 3a, Figure 4a) and aggregate fraction (Figure 4c) between MAPLE and spin-cast samples. At all MWs, MAPLE-deposited samples exhibit smaller crystallite/aggregate size despite possessing larger fraction of aggregates. It could be that the fast removal of solvents during the transport process hinders the growth of crystallite/aggregate during MAPLE deposition, resulting in smaller crystallites/aggregates compared to spin-cast samples.

Implications of morphology on in-plane charge carrier transport

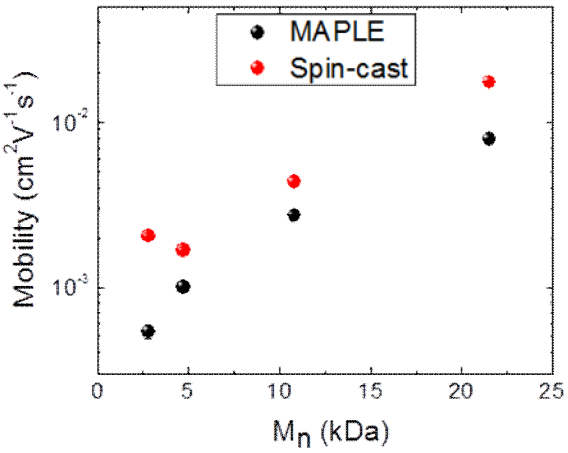

Figure 6: In-plane mobility of spin-cast and MAPLE-deposited samples on OTS-treated SiO_2 substrate as a function of MW.

To understand the role of morphology on carrier transport, we fabricated bottom-gate, top-contact thin-film transistor (TFT) on OTS-treated SiO_2 substrate to study the in-plane transport characteristics of the samples without any post-treatment of the devices such as

annealing. The in-plane mobilities in saturation regime (V_d = -80V) as functions of MW for both MAPLE and spin-cast samples are shown in Figure 6. The transfer characteristics from which hole mobility were extracted are shown in the Supporting Information. At all MWs, the mobilities of MAPLE-deposited samples are lower than the spin-cast analogs, consistent with the shorter conjugation length and smaller crystallite size in MAPLE samples. Except for the lowest M_n = 2.8kDa, the in-plane mobilities of spin-cast samples increase with increasing MW, exceeding 10^{-2} $cm^2V^{-1}s^{-1}$ for the highest MW. This observation is well-known and expected. The mobility of carriers in the 2.8 kDa sample show a modest but reproducible enhancement compared to the 4.7 kDa samples, despite having a shorter conjugation length. It is possible that this improvement in mobility was due to the exceptionally crystalline and ordered fiber morphology of the 2.8kDa sample as suggested by AFM and GIWAXS measurements above. On the other hand, MAPLE samples show a more typical monotonic increase of mobility with MW. This is consistent with the AFM measurement suggesting that the molecular arrangement at the macroscopic micrometer scale of MAPLE-deposited samples is similar. Thus the differences in transport properties of MAPLE-deposited samples for different MWs must originate from the molecular arrangement at a more local scale. In other words, the enhanced conjugation length and domain connectivity with increasing MWs should be the dominant factor contributing to the enhanced carrier mobility of high MW materials.

Finally, it is important to note that in our previous publications, we have shown that the in-plane mobilities in the high MW (ca. 20 kDa) MAPLE-deposited samples are superior to those measured in the high MW spin-cast samples.[23,29] However, in this study, the opposite is shown to be true -the in-plane mobilities are higher in the spin-cast samples. This is most likely due to the higher regioregularity (*RR*) and lower *Đ* of the P3HT batches used in this study. As shown in the Supporting Information, increasing the *RR* and reducing *Đ* of P3HT significantly enhances the absorption strength of the aggregate shoulders in spin-cast films, indicating a higher degree of aggregation, leading to higher mobilities. The same effects have little impact on the structure and charge transport properties in MAPLE-deposited samples, as indicated by the similar shapes of absorption spectra and similar values of carrier mobilities.

CONCLUSIONS

We showed that the structures of MAPLE-deposited poly(3-hexylthiophene) films were more disordered than spin-cast P3HT films; details of the structures were moreover molecular weight dependent. This behavior has important implications on the carrier mobilities within these materials. The crystallite sizes along the side-chain direction (100) decreased, whereas the conjugation length increased, with increasing MWs. Additionally, the degree of disorder in the (010) and (100) directions increased with MW, consistent with a higher degree of chain folding in high MW materials. Through a careful analysis of UV-vis absorption spectra, the low MW samples were shown to consist of crystallites/aggregates embedded within a highly disordered amorphous matrix, whereas the high MW samples consisted of long polymer chains that connected the aggregated domains, in agreement with the chain-packing models for conjugated polymers. The implications of the morphology on charge transport were illustrated by studying the evolution of field-effect mobility as a function of MWs. Larger carrier mobilities measured in the higher MW samples are consistent with this notion -the importance of domain connectivity both at local and macroscopic scale regarding TFT transport. The lower carrier mobilities in the MAPLE-deposited samples are consistent with the shorter conjugation length that characterizes their structures. Our results highlight the strong connection between

chemistry, processing, morphology and charge transport in conjugated polymers thin films.

ACKNOWLEDGEMENTS

B.X.D acknowledges partial financial support from Vietnam Education Foundation and the University of Michigan. We acknowledge partial support from the National Science Foundation (NSF), Division of Materials Research (DMR-1305749). A.J.M and M.L.S acknowledge the Army Research Office for support under W911NF-12-1-0214. G.E.S. acknowledges financial support from the National Science Foundation under Grant No. DMR-1151468. This research used resources of the Advanced Photon Source, an Office of Science User Facility operated for the U.S. Department of Energy (DOE) by Argonne National Laboratory under Contract No. DE-AC02-06CH11357.

SUPPORTING INFORMATION

Polymer synthesis procedure, details of Williamson-Hall analysis, Spano and Gierschner analysis, effect of benzyl alcohol on absorption spectra of P3HT solution, effect of regioregularity and PDI of P3HT on absorption spectra of P3HT thin films, TFT transfer characteristics curves are shown in the Supporting Information.

REFERENCES AND NOTES

(1) Borsenberger, P. M.; Weiss, D. S. *Organic Photoreceptors for Xerography*; CRC Press: New York, 1998.

(2) Geffroy, B.; le Roy, P.; Prat, C. *Polym. Int.* **2006**, *55* (6), 572–582.

(3) Müllen, K.; Scherf, U. *Organic Light Emitting Devices: Synthesis, Properties and Applications*; Wiley: New York, 2006.

(4) Sirringhaus, H. *Adv. Mater.* **2014**, *26* (9), 1319–1335.

(5) Günes, S.; Neugebauer, H.; Sariciftci, N. S. *Chem. Rev.* **2007**, *107* (4), 1324–1338.

(6) Kroon, R.; Lenes, M.; Hummelen, J. C.; Blom, P. W. M.; de Boer, B. *Polym. Rev.* **2008**, *48* (3), 531–582.

(7) Bao, Z.; Dodabalapur, A.; Lovinger, A. J. *Appl. Phys. Lett.* **1996**, *69* (26), 4108.

(8) Kline, R. J.; Mcgehee, M. D.; Kadnikova, E. N.; Liu, J.; Fre, J. M. J.; Toney, M. F. *Macromolecules* **2005**, 3312–3319.

(9) Sirringhaus, H.; Brown, P. J.; Friend, R. H.; Nielsen, M. M.; Bechgaard, K.; Langeveld-Voss, B. M. W.; Spiering, A. J. H.; Janssen, R. A. J.; Meijer, E. W.; Herwig, P.; de Leeuw, D. M. *Nature* **1999**, *401* (6754), 685–688.

(10) Chang, J.-F.; Sun, B.; Breiby, D. W.; Nielsen, M. M.; Sölling, T. I.; Giles, M.; McCulloch, I.; Sirringhaus, H. *Chem. Mater.* **2004**, *16* (23), 4772–4776.

(11) Li, A.; Bilby, D.; Dong, B. X.; Amonoo, J.; Kim, J.; Green, P. F. *J. Polym. Sci. Part B Polym. Phys.* **2015**, *54*, 180–188.

(12) Dong, B. X.; Amonoo, J. A.; Purdum, G. E.; Loo, Y. L.; Green, P. F. *ACS Appl. Mater. Interfaces* **2016**, *8* (45), 31144–31153.

(13) Mcgi, R. A.; Chriseya, D. B.; Piqué, A.; Misnac, T. E.; Washington, D. C. *Laser Appl. Microelectron. Optoelectron. Manuf. III* **1998**, *3274*, 255–266.

(14) Piqué, a.; McGill, R. a.; Chrisey, D. B.; Leonhardt, D.; Mslna, T. E.; Spargo, B. J.; Callahan, J. H.; Vachet, R. W.; Chung, R.; Bucaro, M. a. *Thin Solid Films* **1999**, *355*, 536–541.

(15) Chrisey, D. B.; Piqué, A.; McGill, R. A.; Horwitz, J. S.; Ringeisen, B. R.; Bubb, D. M.; Wu, P. K. *Chem. Rev.* **2003**, *103* (2), 553–576.

(16) Shepard, K. B.; Priestley, R. D. *Macromol. Chem. Phys.* **2013**, *214* (8), 862–872.

(17) Shepard, K. B.; Christie, D. a.; Sosa, C. L.; Arnold, C. B.; Priestley, R. D. *Appl. Phys. Lett.* **2015**, *106* (9), 93104.

(18) Guo, Y.; Morozov, A.; Schneider, D.; Chung, J. W.; Zhang, C.; Waldmann, M.; Yao, N.; Fytas, G.; Arnold, C. B.; Priestley, R. D. *Nat. Mater.* **2012**, *11* (4), 337–343.

(19) Jeong, H.; Shepard, K. B.; Purdum, G. E.; Guo, Y.; Loo, Y. L.; Arnold, C. B.; Priestley, R. D. *Macromolecules* **2016**, *49* (7), 2860–2867.

(20) Pate, R.; Lantz, K. R.; Stiff-Roberts, A. D. *IEEE J. Sel. Top. Quantum Electron.* **2008**, *14* (4), 1022–1030.

(21) Ge, W.; McCormick, R. D.; Nyikayaramba, G.; Stiff-Robertsa, A. D. *Appl. Phys. Lett.* **2014**, *104* (22), 223901.

(22) Ge, W.; Li, N. K.; McCormick, R. D.; Lichtenberg, E.; Yingling, Y. G.; Stiff-Roberts, A. D. *ACS Appl. Mater. Interfaces* **2016**, *8* (30), 19494–19506.

(23) Li, A.; Dong, B. X.; Green, P. *MRS Commun.* **2015**, *5* (4), 593–598.

(24) Gutiérrez-Llorente, a.; Horowitz, G.; Pérez-Casero, R.; Perrière, J.; Fave, J. L.; Yassar, a.; Sant, C. *Org. Electron. physics, Mater. Appl.* **2004**, *5* (1–3), 29–34.

(25) McCormick, R. D.; Lenhardt, J.; Stiff-Roberts, A. D. *Polymers (Basel).* **2012**, *4* (4), 341–354.

(26) Mariano, F.; Caricato, A. P.; Accorsi, G.; Leo, C.; Cesaria, M.; Carallo, S.; Genco, A.; Simeone, D.; Tunno, T.; Martino, M.; Gigli, G.; Mazzeo, M. *J. Mater. Chem. C* **2016**, *4* (3), 7667–7674.

(27) Caricato, a. P.; Cesaria, M.; Gigli, G.; Loiudice, a.; Luches, a.; Martino, M.; Resta, V.; Rizzo, a.; Taurino, a. *Appl. Phys. Lett.* **2012**, *100* (7), 73306.

(28) Ge, W.; Atewologun, A.; Stiff-Roberts, A. D. *Org. Electron. physics, Mater. Appl.* **2015**, *22*, 98–107.

(29) Dong, B. X.; Li, A.; Strzalka, J.; Stein, G. E.; Green, P. F. *J. Polym. Sci. Part B Polym. Phys.* **2017**, *55* (1), 39–48.

(30) Stiff-roberts, A. D.; Ge, W. *Appl. Phys. Rev.* **2017**, *4*, 41303.

(31) Dong, B. X.; Strzalka, J.; Jiang, Z.; Li, H.; Stein, G. E.; Green, P. F. *ACS Appl. Mater. Interfaces* **2017**, *9*, 44799–44810.

(32) Wenderott, J. K.; Dong, B. X.; Green, P. F. *J. Mater. Chem. C* **2017**, *5*, 7446–7451.

(33) Iovu, M. C.; Sheina, E. E.; Gil, R. R.; McCullough, R. D. *Macromolecules* **2005**, *38* (21), 8649–8656.

(34) Bryan, Z. J.; McNeil, A. J. *Macromolecules* **2013**, *46* (21), 8395–8405.

(35) Leone, A. K.; McNeil, A. J. *Acc. Chem. Res.* **2016**, *49* (12), 2822–2831.

(36) Palermo, E. F.; McNeil, A. J. *Macromolecules* **2012**, *45* (15), 5948–5955.

(37) Jiang, Z.; Li, X.; Strzalka, J.; Sprung, M.; Sun, T.; Sandy, A. R.; Narayanan, S.; Lee, D. R.; Wang, J. *J. Synchrotron Radiat.* **2012**, *19* (4), 627–636.

(38) Jiang, Z. *J. Appl. Crystallogr.* **2015**, *48* (3), 917–926.

(39) Koch, F. P. V.; Heeney, M.; Smith, P. *J. Am. Chem. Soc.* **2013**, *135* (37), 13699–13709.

(40) Koch, F. P. V.; Rivnay, J.; Foster, S.; Müller, C.; Downing, J. M.; Buchaca-Domingo, E.; Westacott, P.; Yu, L.; Yuan, M.; Baklar, M.; Fei, Z.; Luscombe, C.; McLachlan, M. A.; Heeney, M.; Rumbles, G.; Silva, C.; Salleo, A.; Nelson, J.; Smith, P.; Stingelin, N. *Progress in Polymer Science*. 2013, pp 1978–1989.

(41) Himmelberger, S.; Duong, D. T.; Northrup, J. E.; Rivnay, J.; Koch, F. P. V.; Beckingham, B. S.; Stingelin, N.; Segalman, R. a.; Mannsfeld, S. C. B.; Salleo, A. *Adv. Funct. Mater.* **2015**, *25* (17), 2616–2624.

(42) Joshi, S.; Pingel, P.; Grigorian, S.; Panzner, T.; Pietsch, U.; Neher, D.; Forster, M.; Schere, U. *Macromolecules* **2009**, *42* (13), 4651–4660.

(43) Joshi, S.; Joshi, S.; Grigorian, S.; Grigorian, S.; Pietsch, U.; Pietsch, U.; Pingel, P.; Pingel, P.; Zen, A.; Zen, A.; Neher, D.; Neher, D.; Scherf, U.; Scherf, U. *Macromolecules* **2008**, *41* (18), 6800–6808.

(44) Rivnay, J.; Noriega, R.; Kline, R. J.; Salleo, A.; Toney, M. F. *Phys. Rev. B - Condens. Matter Mater. Phys.* **2011**, *84* (4), 1–20.

(45) Duong, D. T.; Ho, V.; Shang, Z.; Mollinger, S.; Mannsfeld, S. C. B.; Dacuña, J.; Toney, M. F.; Segalman, R.; Salleo, A. *Adv. Funct. Mater.* **2014**, *24* (28), 4515–4521.

(46) Smilgies, D. M. *J. Appl. Crystallogr.* **2009**, *42* (6), 1030–1034.

(47) Noriega, R.; Rivnay, J.; Vandewal, K.; Koch, F. P. V; Stingelin, N.; Smith, P.; Toney, M. F.; Salleo, A. *Nat. Mater.* **2013**, *12* (11), 1038–1044.

(48) Mena-osteritz, E.; Meyer, A.; Langeveld-voss, B. M. W.; Janssen, R. A. J.; Meijer, E. W.; Bäuerle, P. *Angew. Chemie Int. Ed.* **2000**, No. 15, 2679–2684.

(49) Brinkmann, M. *J. Polym. Sci. Part B Polym. Phys.* **2011**, *49* (17), 1218–1233.

(50) Clark, J.; Silva, C.; Friend, R.; Spano, F. *Phys. Rev. Lett.* **2007**, *98* (20), 206406.

(51) Spano, F. C. *J. Chem. Phys.* **2005**, *122* (23), 234701.

(52) Spano, F. C. *Chem. Phys.* **2006**, *325* (1), 22–35.

(53) Gierschner, J.; Huang, Y.-S.; Van Averbeke, B.; Cornil, J.; Friend, R. H.; Beljonne, D. *J. Chem. Phys.* **2009**, *130* (4), 44105.

(54) Scharsich, C.; Lohwasser, R. H.; Sommer, M.; Asawapirom, U.; Scherf, U.; Thelakkat, M.; Neher, D.; Köhler, A. *J. Polym. Sci. Part B Polym. Phys.* **2012**, *50* (6), 442–453.

(55) Clark, J.; Chang, J.-F.; Spano, F. C.; Friend, R. H.; Silva, C. *Appl. Phys. Lett.* **2009**, *94* (16), 163306.

(56) Kim, B. G.; Kim, M. S.; Kim, J. *ACS Nano* **2010**, *4* (4), 2160–2166.

(57) Choi, D.; Chang, M.; Reichmanis, E. *Adv. Funct. Mater.* **2015**, *25* (6), 920–927.

(58) Zen, a.; Pflaum, J.; Hirschmann, S.; Zhuang, W.; Jaiser, F.; Asawapirom, U.; Rabe, J. P.; Scherf, U.; Neher, D. *Adv. Funct. Mater.* **2004**, *14* (8), 757–764.

(59) Jimison, L. H.; Himmelberger, S.; Duong, D. T.; Rivnay, J.; Toney, M. F.; Salleo, A. *J. Polym. Sci. Part B Polym. Phys.* **2013**, *51* (7), 611–620.

(60) Duong, D. T.; Toney, M. F.; Salleo, A. *Phys. Rev. B* **2012**, *86* (20), 205205.

(61) Shepard, K. B.; Arnold, C. B.; Priestley, R. D. *ACS Macro Lett.* **2014**, *3* (10), 1046–1050.

(62) Leveugle, E.; Zhigilei, L. V. *J. Appl. Phys.* **2007**, *102* (7), 1–19.